Structural defects in compounds ZnXSb (X = Cr, Mn, Fe): Origin of disorder and its relationship with electronic properties

Kamil Ciesielski,[1,2,*] Lídia C. Gomes,[3,4] Grace A. Rome,[1] Erik A. Bensen,[1] Jesse M. Adamczyk,[1] Dariusz Kaczorowski,[2] Elif Ertekin,[3,5] and Eric S. Toberer[1,†]

[1]*Physics Department, Colorado School of Mines, Golden, Colorado 80401, USA*
[2]*Institute of Low Temperature and Structure Research, Polish Academy of Sciences, 50-422 Wrocław, Poland*
[3]*University of Illinois at Urbana-Champaign, Urbana, Illinois 61820, USA*
[4]*Instituto de Física Teórica, São Paulo State University (UNESP), São Paulo 01049-010, Brazil*
[5]*National Center for Supercomputing Applications, Urbana, Illinois 61801, USA*

(Received 11 March 2022; revised 8 April 2022; accepted 20 April 2022; published 21 June 2022)

Crystallographic disorder is known to be crucial for the understanding of transport properties of intermetallic compounds. ZrSiS-type phases with the general formula ZnXSb, where X is a transition metal, are recognized for their extraordinarily large amount of structural defects. Here, we explain the origin of the disorder and investigate its influence on the electronic behavior of ZnCrSb, ZnMnSb, and ZnFeSb. Synchrotron diffraction data revealed substantial amounts of vacancies on the transition-metal sites for all three compounds. Based on bonding analysis and calculations of crystal orbital Hamilton population (COHP), we claim that the defects originate from antibonding interactions on a two-dimensional square sublattice formed by X atoms. To test our thesis, we compare the ZrSiS-type materials with the chemically similar phase, ZnNiSb, which crystallizes in the MgAgAs-type cell. In this structure, the closest X-X distance is almost doubled with respect to the ZrSiS-type counterparts. In concert with expectations, the COHP calculation for ZnNiSb does not show an X-X antibonding interaction, and virtually no defects are detectable via the experimental diffraction analysis. From the perspective of electron transport, ZrSiS-type compounds were characterized by a residual resistivity ratio (*RRR*) that was significantly lower than that of ZnNiSb, which indicates stronger point-defect scattering of electrons in our disordered compounds. At the lowest temperatures, we also observed, for ZrSiS-type compounds, signatures of another phenomenon known exclusively for disordered metallic conductors: the Altshuler-Aronov (AA) correction to Coulomb interaction. The effect is not present for the defect-free compound ZnNiSb. ZnFeSb shows the lowest *RRR* and the highest onset temperature of the AA effect. Furthermore, heat-capacity studies revealed order of magnitude enhancement of Sommerfeld coefficient for ZnFeSb with respect to the value obtained from *ab initio* density of states calculations. This finding might be correlated to the structural instability. The presented analysis can be useful for understanding materials in which structural disorder significantly affects the electronic properties.

DOI: 10.1103/PhysRevMaterials.6.063602

I. INTRODUCTION

Understanding crystallographic disorder is frequently considered to be vital for further growth in materials science [1,2]. One of the examples is the field of thermoelectrics, where crystallographic defects are commonly found to be beneficial due to the demand of simultaneous low thermal conductivity and good mobility of charge carriers [3–9]. ZrNiSn can serve as an interesting case study, where its Ni interstitials act as efficient scattering centers for phonons, while leaving the electron transport virtually unharmed. Indifference of charge carriers to disorder can be explained by the intrinsically low mean free path of electrons in ZrNiSn [3]. The photovoltaic community, in turn, seeks to precisely control the amount of lattice imperfections, as too many defects can easily hamper device performance [10–12]. Disorder also seems to gather considerable attention in the basic sciences research community, typically due to its influence on superconductivity [13–16] and topological properties [17–20]. Interestingly, despite the ability to detect crystallographic imperfections more and more precisely, studies aimed at understanding the origin of the disorder are still rather uncommon.

To advance our understanding of disorder in intermetallic compounds, we take a case study of compounds with ZrSiS-type structure ($P4/nmm$, no. 129). Many of them are known to exhibit significant atomic disorder [21–23], which is accompanied by a variety of unconventional magnetotransport properties that may be affected or related to the defects. These include the presence of tunneling states leading to two-channel Kondo behavior [21], superconductivity [24], topological properties [25], and fractional metal-insulator transition [22]. In this article, we focus on a narrow group with a general composition of ZnXSb, where X is a metal from the third row of the periodic table. The known compounds

*kciesielski@mines.edu
†etoberer@mines.edu

are ZnVSb [22], ZnMnSb [26], and ZnFeSb [27]. In between the series Zn*X*Sb, X = V–Fe, we encounter uncharted territory with X = Cr. To the best of our knowledge, its only literature mention is the appearance of 1-1-1–like (ZnCrSb-like) precipitations in energy-dispersive X-ray analysis of $Zn_{13}Sb_{10}$ doped with Cr [28].

ZrSiS-type compounds are known to exhibit a significant amount of point defects in their crystal structure. The recent discovery of ZnVSb revealed vacancies on vanadium and antimony sites (9.4% for V and 6.1% for Sb) [22]. For the next compound from the series, ZnMnSb, the structural analysis also indicated a large amount of imperfections: vacancies on Mn and Zn sites (11.1% for Mn, 3.6% for Zn) [26]. ZnFeSb was first reported to attain the cubic MgAgAs-type structure ($F\bar{4}3m$, no. 216) [27]. Later on, however, it was shown that the 1-1-1–like compositions may also crystallize in two other forms depending on the thermal treatment: ZrSiS-type structure, and $2 \times 2 \times 2$ distorted supercell of MgAgAs-type structure ($Fm\bar{3}m$, no. 225) [29], isotypic with $Ru_9Zn_7Sb_8$ [30]. The dominant defects in the ZrSiS-type cell were vacancies on the iron site, ranging from 8% to 12% depending on the studied crystal. The near-stoichiometric variant of ZnFeSb crystallizing in the supercell exhibits vacancies on selected Fe and Zn sites, the final composition being $Fe_{7.87}Zn_{6.72}Sb_8$ [29]. To date, the reason for the emergence of such significant disorder has not been addressed.

From an electrical perspective, the considered group of materials are "bad metals." The electrical resistivity of ZnVSb exhibits complex semimetaliclike temperature behavior, with values at room temperature, $\rho_{300K} = 9.6\ \mu\Omega$m [22]. In the range of 120–160 K, ρ shows magnetic-field-independent hysteresis, which appears to be a signature of a partial metal-insulator transition. The electronic band structure of the material shows a narrow pseudogap in the proximity of the Fermi level. The resistivity of ZnMnSb is nearly temperature independent and displays a semimetalliclike behavior with value of $\rho_{300K} \approx 50\ \mu\Omega$m [26]. ZnFeSb in the ZrSiS-type structure showed weakly temperature-dependent resistivity with value of approximately 145 $\mu\Omega$m at 300 K [29]. The temperature cycling of this compound revealed some unrepeatability, which might be related to an incomplete densification process of the studied pellet.

As shown in Ref. [31], the entire family of ZrSiS-like compounds can be approached as partially itinerant magnetic systems. ZnVSb comprises both itinerant and localized magnetic contributions [22]. A combination of chemical bonding analysis, band structure calculations, magnetotransport measurements, and x-ray photoemission spectroscopy revealed that the itinerant electrons arise from vanadium atoms exhibiting V-V orbital overlap. Fractional localization, in turn, stems from V atoms adjoining vacancies, which hinder orbital overlap. The value of a localized magnetic moment for ZnVSb is very small ($0.25\mu_B$). ZnMnSb was reported as a high-temperature ferromagnet, $T_C = 302$ K. The magnetic moment on Mn atoms was shown to attain surprisingly low values ($\mu_{\text{eff}} = 1.2-1.6\ \mu_B$ [26,32]), much smaller than expected for a localized Mn atom in the most common d^5 configuration ($5.92\ \mu_B$). This low μ_{eff} was explained as possibly stemming from the unusual d^6 spin configuration of Mn [26] or delocalized character of magnetism [32,33]. The authors of Ref. [29] indicated the ferromagnetic ordering of ZnFeSb in a ZrSiS-type variant at 275 K with a moment of $1.95\mu_B$ per Fe atom, which is close to the expected value for iron in a body-centered-cubic environment ($2.22\ \mu_B$/Fe atom). No repeatable anomaly in resistivity corresponding to that suggested by the authors' magnetic ordering was observed though. At lower temperatures (approximately 30 K), the magnetization of ZnFeSb exhibited signatures similar to that of spin-glass systems.

In a short summary of the literature, Zn*X*Sb compounds crystallizing in a ZrSiS-type structure show a strong tendency towards crystallographic disorder. Vacancies on the X site are the dominant defects; however, the origin of the defect has not been rationalized, to date. A variety of unconventional properties in these materials appears to be closely related to the presence of these structural imperfections. Hence, we decided to meticulously study the source of disorder in compounds Zn*X*Sb, X = Cr, Mn, Fe; with ZnCrSb being a newly discovered material. Our techniques include band structure and magnetic ordering energy calculations, crystal orbital Hamilton population (COHP) formalism, as well as measurements of synchrotron diffraction, electrical resistivity, magnetoresistance, heat capacity, and magnetic susceptibility. By combining a variety of theoretical and experimental tools, we aim to clarify the possible interplay between structural peculiarities and electrical transport of the studied materials.

II. METHODS

A. Experimental methods

Polycrystalline samples of Zn*X*Sb compounds were synthesized from elements purchased from Alfa Aesar: Zn (flake, 99.9 at.%), Cr (powder, 99.99 at.%), Mn (chunks, 99.9 at.%), Fe (granules, 99.98 at.%), and Sb (shot, 99.999 at.%). Each synthesis step was performed in a nitrogen-filled glove box ($O_2 < 1$ ppm, $H_2O < 1$ ppm). Elemental constituents were sealed under inert gas and ball milled for 90 min in a high-energy ball mill Spex 8000D. Two tungsten carbide balls with a 12 mm diameter were used against the 10 g summed mass of the elements.

The obtained powders were sealed under vacuum in silica tubes and annealed at 550 °C with a ramping time of 5 hours; the maximum temperature was maintained for 24 hours. After the furnaces were turned off and reached the room temperature, the silica tubes were removed to air, and powder products were hand ground in an agate mortar with subsequent sieving through a 106 μm mesh. The so-obtained samples were enclosed in Kapton capillaries and sent for the remote X-rays powder diffraction (XRD) measurements at the Advanced Photon Source (APS) beam line 11-BM. Rietveld refinement was performed with FULLPROF software [34].

For transport and thermodynamic properties, we densified approximately 2.5 g of the powders by hot pressing in an induction-heated graphite die. The conditions of the synthesis were $T_{\max} = 550$ °C, $p = 20$ MPa, while the environment was a dynamic vacuum with pressure below 5 mTorr. The temperature $T_{\max}$ was maintained for at least 6 hours.

Electrical resistivity (ρ) and heat capacity (C_p) experiments were performed with the Physical Property Measurement

System (PPMS, Quantum Design) equipped with a 9 T magnet. For ρ measurements, we cut the samples into a rectangular shape and prepared an electrical contact on polished surfaces with silver paste and Ag wires (50 μm diameter). The C_p investigation was performed employing the relaxation method with the two-τ model. Magnetic susceptibility experiments were carried out on the Magnetic Property Measurement System (SQUID, Quantum Design) with a 7 T magnet.

B. Calculations

The calculations were carried out using density functional theory (DFT), as implemented in the Vienna Ab initio Simulation Package (VASP) [35]. The generalized gradient approximation (GGA) of the Perdew-Burke-Ernzerhof (PBE) approach [36], as well as the projector augmented wave formalism [37], were employed. We expanded the Kohn-Sham orbitals with a plane-wave basis with a cutoff energy of 520 eV. Atomic positions and lattice parameters were refined until forces converged to values lower than 1 meV/Å per atom. High consistency between theoretical and experimental structural parameters was achieved. The same set of lattice vectors and atomic positions was used in all performed calculations. The atomic positions are assumed to be fully occupied. Sampling of the Brillouin zone was performed with a Γ-centered $8 \times 8 \times 4$ Monkhorst-Pack k-point grid [38]. A finer mesh of $12 \times 12 \times 10$ k points was used for the calculation of the total and partial density of states (DOS and pDOS). These were plotted with the Sumo PYTHON toolkit [39]. For all calculations, a Hubbard-like U parameter [40] was used to treat the on-site Coulomb interactions on the localized d orbitals. The U values are equal to +3 eV to the transition metals X, and +6 eV for Zn. These values were chosen based on our previous work for ZnVSb [22]. There, we checked the typical range of the parameter U for V and Zn in the previous literature: 0, +3, and +5 eV for vanadium and +5, +6, and +7 eV for zinc [41–44]. The eventual values of U were chosen based on a comparison of the theoretical density of states with experimental x-ray photoemission spectroscopy results [22].

Crystal orbital Hamilton population (COHP) [45,46] analysis was used to investigate the nature of bonds in the compounds and was calculated using the LOBSTER code [47]. COHP values between two atoms can be obtained by partitioning the (k-dependent) wave function, pregenerated from a self-consistent DFT calculation, into bonding, nonbonding, and antibonding contributions. For such, the plane-wave basis set used in VASP must be transformed to a localized basis set of the Slater-type orbitals (STOs), as proposed by Maintz [48]. COHP is then defined as

$$-\mathrm{COHP}_{ij}(E) = H_{ij} \sum_n c_i^n c_j^{*n} \delta(E - E_n), \qquad (1)$$

where H_{ij} is the Hamilton matrix element between atomic orbitals ϕ_i and ϕ_j, and c_i^n are the coefficients associated with ϕ_i in a molecular orbital, $\Psi_n = \sum c_i^n \phi_i$.

In a COHP diagram, $-\mathrm{COHP}_{ij}(E)$ values between two atoms are plotted as a function of energy (similarly to a density of states plot). The minus sign is usually added to make such plot more intuitive, so that positive, negative, and zero values indicate bonding, antibonding, and nonbonding interactions, respectively. The obtained charge spilling magnitude is small: 1.90% for ZnCrSb, 2.54% for ZnFeSb, 2.49% for ZnMnSb, and 2.57% for ZnNiSb. Conventionally, values below 5% in LOBSTER code are considered reliable.

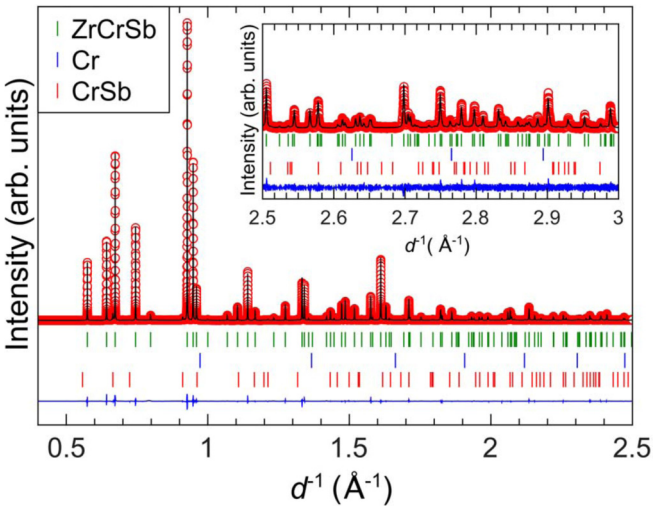

FIG. 1. Results of Rietveld refinement for ZnCrSb. The green ticks denote the main phase ZnCrSb, while blue and red ticks shown in the legend correspond to the minuscule amount of the impurity phases: Cr and CrSb, respectively.

III. RESULTS

A. Experimental crystal structure

The exemplary results for ZnCrSb are displayed in Fig 1. For the XRD plots of the compounds ZnXSb, X = Fe, Mn, Ni, the reader is referred to Figs. S1– S3 in the Supplemental Material (SM) [49]. Unit-cell parameters resulting from the Rietveld analysis and technical details are collected in Table S1, while atomic data and selected interatomic distances are quantified in Tables S2 and S3, respectively. Our Rietveld refinement showed that ZnCrSb, ZnFeSb, and ZnMnSb attained a ZrSiS-type unit cell, while ZnNiSb was successfully analyzed in a MgAgAs-type structure—the commonly known prototype for half-Heusler phases. ZnCrSb is the newly discovered compound. Lattice parameters for the known materials (ZnFeSb, ZnMnSb, ZnNiSb) are in good agreement with the literature [26,29,50,51].

The ZrSiS-type cell [Fig. 2(a)] is constructed from layers of X atoms arranged in squares, which are separated by Zn-Sb rock-salt-like slabs. The deviation of Zn-Sb units from ideal cubes is driven by the nonuniformity of horizontal and vertical Zn-Sb distances and gentle distortion of angles from 90° (see Table S3 in the SM [49]). The transition-metal atoms X are coordinated by four other X atoms in-plane; they form a square two-dimensional (2D) sublattice. The second-nearest neighbors are four Zn and four Sb atoms [see Fig. 2(b)]. In the half-Heusler phase [Fig. 2(c)], the ZnSb rock-salt units are unperturbed from the ideal cubic arrangement. Ni atoms are rather far away from each other, located in voids coordinated by four Zn and four Sb atoms.

For all the compounds, we checked the data against the possibility of vacancies on each Wyckoff site. A considerable

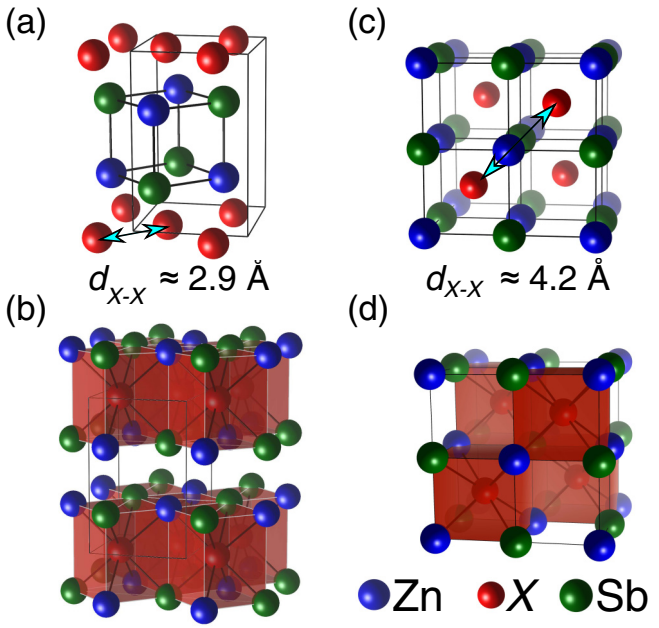

FIG. 2. Crystal structures of ZrSiS type with (a) the elementary cell, (b) Zn-Sb rock-salt-like polyhedra, and (c) MgAgAs-type unit cell, with its version with (d) Zn-Sb polyhedra.

amount of defects on X atom sites was found for ZnXSb, X = Cr, Mn, Fe, (cf. Table S2 in the SM [49] and Fig. 3). Additionally, we find some small amounts of Zn deficiency in all three ZrSiS-type phases. For each compound, we also checked the data against all possibilities of antisite disorder and we found mixed occupancy on the Zn-Sb sublattice for the ZrSiS-type phases. The best results were obtained when vacancies on the X site were combined with Zn-Sb antisite defects. The amount of antisite defects fluctuated around 5% on each (Zn/Sb) site. Since it is impossible to distinguish from the two models based solely on synchrotron diffraction data, we decided to stick with a simpler structural approach: only X and Zn vacancies were allowed. Lastly, the ZnNiSb was found to be an almost perfectly ordered material; only a

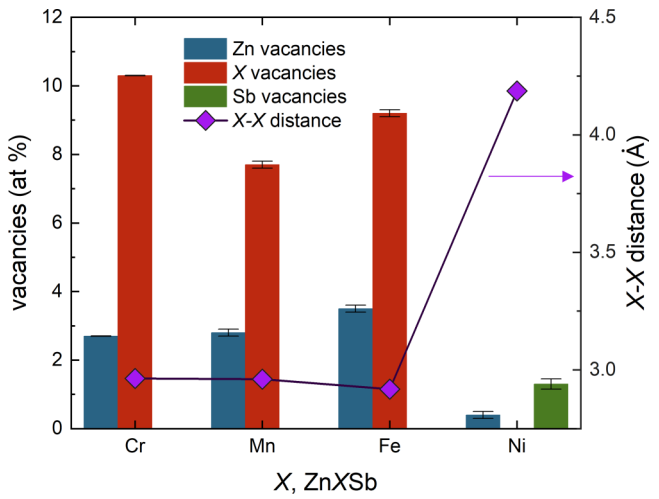

FIG. 3. Summary graph of crystallographic defects in ZnXSb phases.

minuscule amount of vacancies on Zn and Sb (<3%) sites was detected.

Isotropic displacement parameters (Table S2 in the SM [49]) are very similar for phases ZnXSb, X = Cr, Mn, and rise for ZnFeSb. This feature might be correlated to structural instability. ZnFeSb is known to attain three polymorphic modifications in the proximity of 1-1-1 stoichiometry [29] (see Sec. I). ZnNiSb shows strongly reduced B_{iso} parameters, which along with decent crystallographic order, further supports the view of this compound as the most stable phase from the series. Crystallographic density rises with heavier transition metals in the ZnXSb series (cf. Table S1 in the SM [49]).

After taking a closer look at angles and interatomic distances (Table S2 in the SM [49]), it is easy to notice two tendencies. First, the closest X-X atoms distance is similar for compounds ZnXSb, X = Cr–Fe (approximately 2.9 Å), yet in the ordered ZnNiSb, the close X-X atomic arrangement is no longer present. The shortest X-X separation in ZnNiSb is 4.2 Å; see Fig. 2. The discussed difference (i.e., close X-X bonding in compounds with ZrSiS-type structure and lack of thereof in ZnNiSb) might be correlated with a large amount of vacancies on the X site occurring only in the ZrSiS-type structure. As a second trend, we notice that the distortion in angles from 90° rises from ZnCrSb up to ZnFeSb. Eventually, for ZnNiSb, the Zn-Sb-Zn angle is defined by the symmetry of the system as 90°, which might reflect tension in the crystal units being a driving force for structural transformations.

ZnNiSb will serve as a good verification of the hypothesis on disorder in compounds ZnXSb, X = Cr, Mn, Fe, crystallizing in the ZrSiS-type structure. ZnNiSb has no close X-X bonds, as opposed to ZrSiS-type compounds, which in the latter case are expected to be the driving factor for the occurrence of X vacancies. However, many other features of ZnNiSb are similar to the ZrSiS-type structure. From the perspective of chemical composition, two of the three constituent atoms (Zn, Sb) are present in ZnNiSb as well as ZrSiS-type materials; the differentiating Ni atom is in close proximity to the heaviest ZrSiS-type compound, ZnFeSb, X = Fe; nickel is just two electrons heavier than iron. The Zn-Sb arrangement (type of polyhedra—red building blocks on Fig. 2) is similar to all the studied compounds, as are the Zn-X and Sb-X bonds; see Table S3 in the SM [49]. Last, but not least, the size of the unit cell is of the same order of magnitude, which excludes the possibility of influencing the transport properties by the complexity that could be present, e.g., due to large supercells.

In the next paragraph, we will compare the current results with the existing literature data. Our report on disorder is consistent with previous data on ZnMnSb which showed approximately 10% vacancies on the Mn site [26]. The authors of Ref. [26] also considered an alternative disorder scenario: vacancies on Mn and Zn sites (11.1% for Mn, 3.6% for Zn), or a strong tendency towards Mn-Zn antisite defect formation (nominal Zn site: 65% of Zn, 35% Mn; nominal Mn site: 57% Mn, 27% Zn, 16% vacancies). Subsequent neutron diffraction studies from the literature for ZnMnSb, however, suggested that the structural model with vacancies only is more likely [52]. Furthermore, a recently reported study using electron diffraction suggested the possibility of deviation of the original ZrSiS-type cell of ZnMnSb to trigonal symmetry

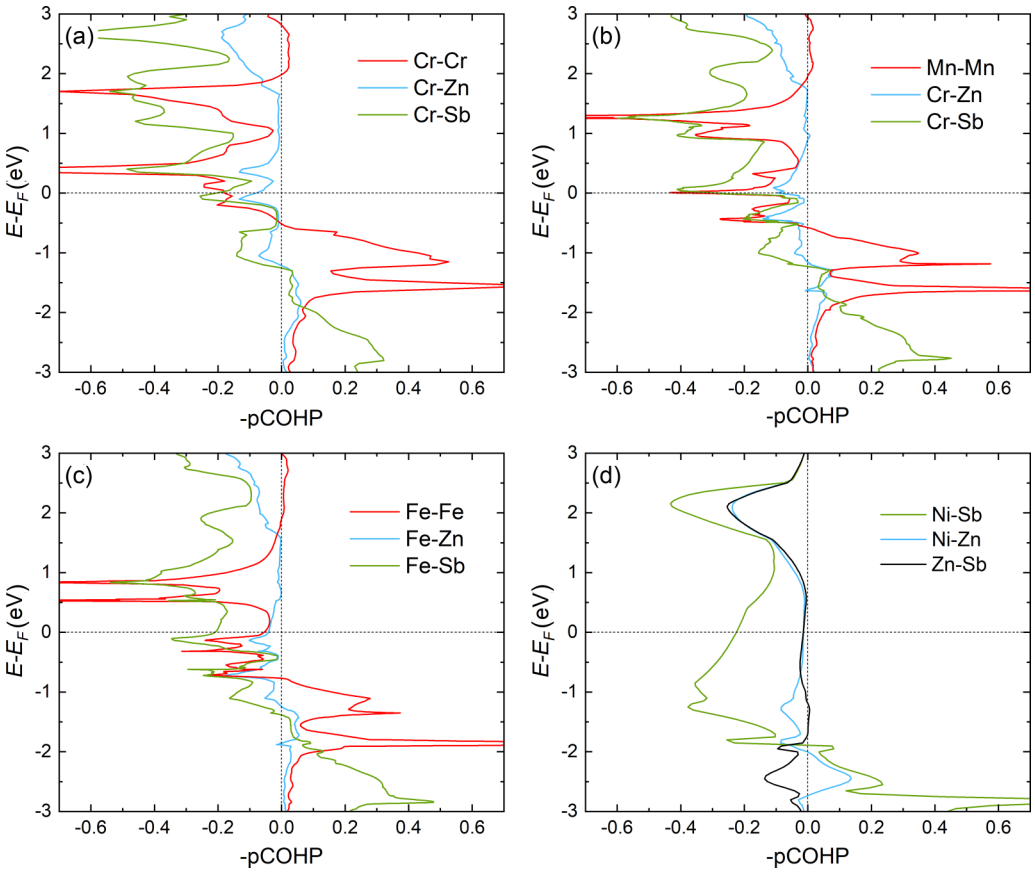

FIG. 4. COHP computed for the X-Zn, X-X, and X-Sb bonds for (a) ZnCrSb, (b) ZnMnSb, (c) ZnFeSb, and (d) ZnNiSb. Curves on the right (left) indicate bonding (antibonding) states. The calculations were performed in an experimental crystal structure observed for the compounds: (a)–(c) ZrSiS type and (d) MgAgAs type.

[32]. No space group or atomic positions were provided [32], though, indicating that possible structural subtleties of ZnMnSb need even more sophisticated techniques to be clarified. In the case of ZnFeSb, a similar amount of vacancies was found on the Fe site in the literature studies [29] compared to this work. Considering the polymorphism of ZnFeSb, the MgAgAs-type structure was previously obtained by arc melting and annealing at 570 K [27], while the supercell of the half-Heusler structure and ZrSiS-type structure were achieved by Xiong *et al.* using the solid-state synthesis of the nonstoichiometric composition Zn:Fe:Sb 0.97:0.91:1 with subsequent annealing in 570 and 873 K, respectively [29]. Our synthesis route and temperatures that were utilized are the closest to those from the literature connected to the ZrSiS-type phase, which explains why this particular structure type is observed for ZnFeSb in our experimental results. Here, it might also be worthwhile comparing the result of structural analysis with the closely related compound ZnVSb crystallizing also in the ZrSiS-type structure [22]. This phase was previously reported to exhibit a slightly different type of structural disorder: vacancies on the transition-metal site were still the dominant defect (9.4%), yet the second type of atomic imperfection was vacancies on the Sb site (4.1%). Also, the electron band structure and experimental magnetotransport properties of ZnVSb are different than those of ZrXSb, X = Cr, Mn, Fe, which will be discussed in the next sections of this article.

Small amounts of impurities were detected in our samples, mostly transition-metal-containing binaries or elemental transition-metal precipitations: 2.27 vol.% CrSb and 0.17 vol.% Cr for ZnCrSb; 0.87 vol.% Mn and 0.27 vol.% Sb for ZnMnSb; 0.95 vol.% Fe_3Zn_{10} and 0.26 vol.% Fe for ZnFeSb; and 6.55 vol.% NiSb for ZnNiSb. Even though each possible elemental, binary, and ternary impurity from the ICSD database was checked, some minuscule Bragg reflections remained unidentified. Those likely correspond to transition-metal-rich impurities, which are expected due to vacancies on the X site in the ZnXSb phases. EDS imaging confirmed the presence of the most prominent impurity phases. Due to the qualitative and local character of EDS imaging, the technique is not used for the discussion of the disorder in the main phase.

To sum up the structural tendencies in the ZnXSb series: for the transition metals X = Cr, Mn, and Fe, the ZrSiS-type structure is observed with the structural instability rising towards a larger mass of the transition-metal atom X. The heaviest material—ZnFeSb—appears to be most unstable from the series based on the large distortions of angles in Zn-Sb cubes, rising B_{iso}, and a significant amount of occupational defects. Furthermore, the existence of three polymorphic modifications of ZnFeSb [29,51] indicates that the compound is on the

verge of structural instability. Eventually, the Zn*X*Sb series finds its way to high symmetry in the half-Heusler phase ZnNiSb with a large *X*-*X* distance, small B_{iso}, and almost no point defects.

B. COHP calculations

Theoretical analysis such as the crystal orbital Hamilton population (COHP) has been successfully used to investigate bonds in solids: in a COHP analysis, the band structure energy is partitioned into orbital-pair interactions, resulting in a "bond-weighted" density of states between pairs of atoms. Based on COHP, one can assess if the interaction between the two considered atoms is bonding, antibonding (energetically unfavorable), or nonbonding (negligible) [45,46]. The method was proven to be effective in explaining the large amount of Ge and Sb vacancies in $Ge_xSb_yTe_4$. In this case, the origin of the disorder turned out to be a tendency of the compound to reduce strong antibonding interactions between Ge-Te and Sb-Te atoms [53]. A somewhat similar situation was reported for $Rh_3Cd_{5-\delta}$, where a large amount of Cd vacancies can be understood as resulting from the need to annihilate the antibonding interactions between Rh and Cd [54].

Figure 4 shows the calculated COHP for Zn*X*Sb, *X* = Cr, Mn, Fe (ZrSiS-type phase), and ZnNiSb (MgAgAs-type phase). For transparency, in Fig. 4 showing compounds in a ZrSiS-type structure, we plot only three bonds involving transition-metal compounds (*X*-*X*, *X*-Zn, and *X*-Sb). The graphs, including all five bonds (i.e., with added Zn-Sb vertical and Zn-Sb horizontal interactions), are in the Supplemental Material, Fig. S4 [49]. The reader is referred to Fig. S5 in the SM [49] for the legend of the bonds plotted in COHP graphs. In the proximity of the Fermi level, all compounds crystallizing in a ZrSiS-type structure show significant half-filled antibonding states (negative COHP values), with the biggest contributions from *X*-*X* and *X*-Sb bonds. The presence of these antibonding states involving the *X* species, a destabilizing contribution, is likely related to the tendency to observe *X* vacancies.

Furthermore, it was shown that structures with large amounts of antibonding states near E_F might exhibit structural distortion towards lower-symmetry unit cells [53]. This feature might be connected to the slight trigonal distortion suggested for ZnMnSb by Murgatroyd *et al.* [32]. Experiments combining more sophisticated techniques such as electron and neutron diffraction, as well as high-resolution electron microscopy, are likely to provide information about further peculiarities in the crystal structure of Zn*X*Sb compounds.

COHP calculations for ZnNiSb [Fig. 4(d)] show that its most significant interaction is between Ni and Sb atoms, which is the second most important bond in ZrSiS-type compounds. Similarly to the case of the disordered Zn*X*Sb compounds, the (*X*=Ni)-Sb interaction in ZnNiSb spans between positive and negative COHP values, being more negative in the proximity of E_F. The *X*-*X* (Ni-Ni) interaction is negligible in ZnNiSb, as expected due to the large spatial separation between these atoms in the MgAgAs-type structure (see Table S3 in the SM [49]). The mutual *X*-*X* bonding, or lack thereof, seem to be of significant importance for vacancy formation at the *X* site in Zn*X*Sb materials (cf. Sec. III A). More quantitative insight into defect-related phenomena in this interesting family of compounds might be obtained by *ab initio* defect energy calculations; see, e.g., Ref. [55].

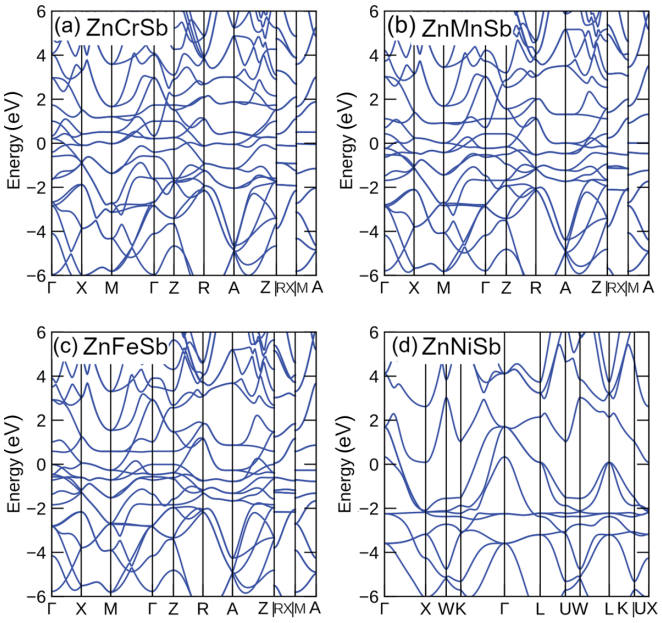

FIG. 5. Electronic band structure of (a) ZnCrSb, (b) ZnMnSb, (c) ZnFeSb, and (d) ZnNiSb. The calculations are performed in the experimental crystal structures: ZrSiS type for ZnCrSb, ZnMnSb, ZnFeSb; and MgAgAs type for ZnNiSb.

Last, but not least we calculated the absolute integral of COHP (iCOHP). The goal of this effort is to attempt to compare iCOHP results with the bonding length. For ZrSiS-type compounds, the iCOHP values are gathered in Fig. S4 in the SM [49], where all five close atomic contacts are plotted, while for ZnNiSb, the iCOHP values are 1.32 eV (Ni-Sb), 0.38 eV (Ni-Zn), and 0.34 eV (Zn-Sb). No clear correlation between iCOHP and the bonding distance (see Table S3 in the SM [49]) could be established. It seems that iCOHP values are influenced by a few factors, and the bonding length is not the clearly dominant one, when the closest bonds are considered.

C. Electronic properties

Calculated electronic band structures are shown in Fig. 5. All the studied Zn*X*Sb compounds are metals with multiple bands crossing the Fermi level (E_F). For ZrSiS-type phases, the *d* orbitals of Cr, Mn, and Fe introduce multiple bands with relatively flat dispersion near E_F. Figure 6 shows the atom-projected density of states (pDOS). All the studied compounds are characterized by finite, sizable DOS at the Fermi level. This feature contrasts another chemically related ZrSiS-type compound, ZnVSb, which exhibits a narrow pseudogap in the vicinity of E_F [22]. A vast majority of the states near E_F for the studied materials originate from *d* orbitals of the transition-metal atoms. States from Zn are strongly localized and located deep below the Fermi level, approximately −10 eV. Antimony in all compounds provides the disperse contribution, which has a wide maximum centered roughly around −2.5 eV below E_F. The dominant contribution to the

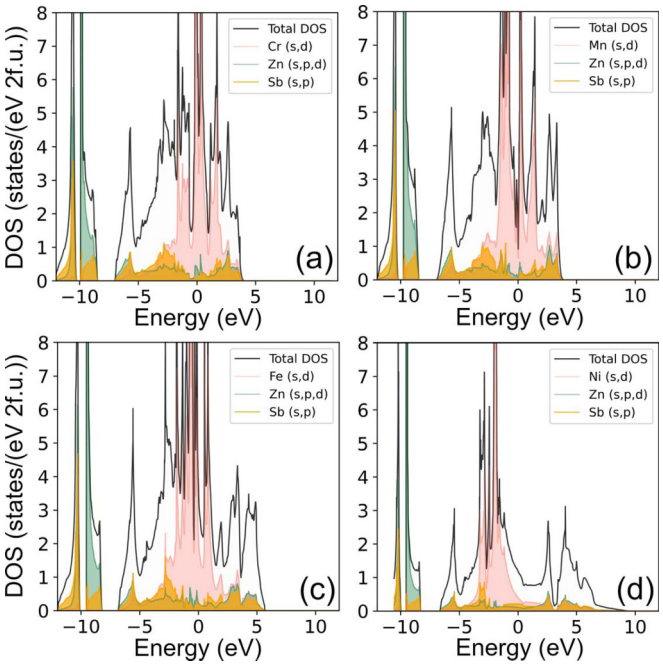

FIG. 6. Atom-projected density of states for (a) ZnCrSb, (b) ZnMnSb, (c) ZnFeSb, and (d) ZnNiSb.

density of states near E_F of the d electrons from the X atoms is confirmed by fat band plots; see Fig. S4 in the SM [49]. The numerical value of the total DOS at E_F for ZnXSb compounds is gathered in Table S4 in the SM [49], while Fig. S6 in the SM [49] presents the pDOS graph projected to separate atomic orbitals (s, p, d) for each atom.

To investigate the possible influence of localized magnetic moment formation on the electronic properties, we also performed calculations of the spin-polarized band structures (see Fig. S8 in the SM [49]). For ZrSiS-type compounds, metallic character with many bands crossing the Fermi level is maintained. The band structure seems to be overall slightly more dispersive (flatter bands) in the spin-polarized mode. For ZnNiSb, the d states from Ni are completely filled, resulting in no magnetization. The orbital DOS in the spin-polarized mode (Fig. S9 in the SM [49]) shows a dominant contribution near E_F of the d states from transition-metal atoms, similar to the calculation in the non-spin polarized mode.

Temperature variations of experimental electrical resistivity (ρ) are displayed in Fig. 7. All the compounds exhibit metallic shapes of ρ. The change of slope observed for ZnMnSb at 312 K corresponds to ferromagnetic ordering, which will be referred to in Sec. III E. Furthermore, phases ZnXSb, X = Cr, Fe, show significant convexity in $\rho(T)$ above 100 K. In the case of ZnCrSb, the effect leads to the formation of a maximum centered at approximately 250 K, while for ZnFeSb, the peak point is probably located above our maximum temperature of measurement (300 K). Wide maxima in resistivity near room temperature are commonly observed in narrow-band-gap semiconductors or semimetals [56–58]. They are often interpreted as a transition from metallic-like extrinsic conductivity to intrinsic charge transfer activation. This scenario, however, cannot be applied to the investigated ZnXSb family due to the considerable density of states at the

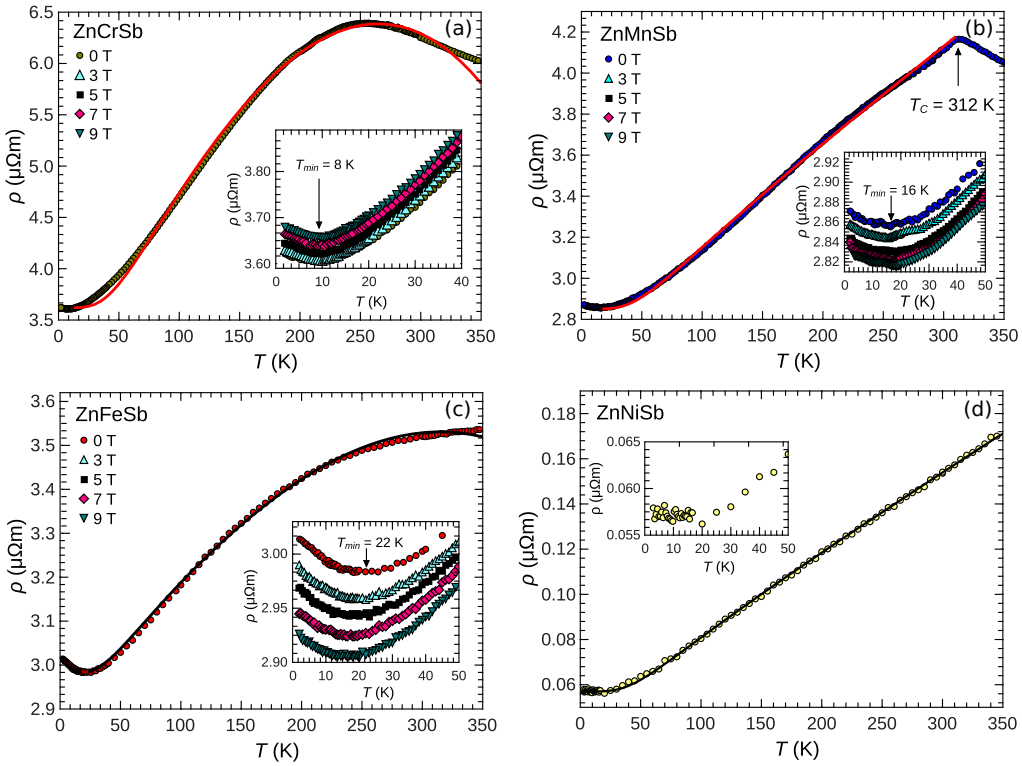

FIG. 7. Temperature dependence of electrical resistivity of (a) ZrCrSb, (b) ZnMnSb, (c) ZnFeSb, and (d) ZnNiSb. Insets to (a)–(c) show measurements performed under different magnetic fields, while the inset to (d) displays the zero-field low-temperature resistivity of ZnNiSb.

TABLE I. Results of electrical resistivity analysis: fit parameters to Eq. (2) (R_{BG}, Θ_R, B), temperature of minimum in resistivity ($T_{\min}$), resistivity at 300 K (ρ_{300K}), and residual resistivity ratio (*RRR*). The numbers in the parentheses are uncertainties obtained from least-square fitting.

Compound	ρ_0 ($\mu\Omega$m)	R_{BG} ($\mu\Omega$m)	Θ_R (K)	B (10^{-8} $\mu\Omega$m K^{-3})	$T_{\min}$ (K)	ρ_{300K} ($\mu\Omega$m)	*RRR*
ZnCrSb	3.62	19.0(3)	270(3)	8.8(1)	8	6.00	1.66
ZnMnSb	2.85	4.95(6)	276(3)		16	4.05	1.36
ZnFeSb	2.97	2.34(9)	212(8)	0.95(1)	22	3.54	1.24
ZnNiSb	0.057	0.34(1)	256(2)			0.17	2.98

Fermi level; cf. Fig. 6. An alternative explanation to this phenomenon might be Mott's interband scattering [59–61]. The effect describes the interaction of s/p and d electrons, which instead of providing two independent conductivity channels, interact destructively on conductivity. Electrons from s or p bands that are expected to have significantly longer mean free paths are no longer contributing to the conductivity as much as they could due to merging into the d band. To qualitatively incorporate Mott's interband scattering into temperature dependence, the common $-BT^3$ term is employed [62–64] as a simplification relevant for low temperatures. The coefficient B is a function of the electronic density of states [60]. For the full derivation of temperature dependence of interband scattering, the readers are referred to the original paper, Ref. [60]. In our least-squares fitting of the resistivity data, the Mott term is combined with the Bloch-Grüneisen equation,

$$\rho(T) = \rho_0 + R_{BG}\left(\frac{T}{\Theta_R}\right)^5 \int_0^{\Theta_R/T} \frac{x^5 dx}{(e^x - 1)(1 - e^{-x})} - BT^3, \tag{2}$$

where Θ_R corresponds to the characteristic cutoff temperature in the phonon spectrum and is frequently regarded as an estimate of the Debye temperature, B denotes a coefficient related to the Mott's interband scattering [60] (see above), and R_{BG} is a parameter related to electron-phonon interactions ($R_{BG} \propto \lambda_{tr}\omega_D/\omega_p$, where λ_{tr} stands for the electron-phonon coupling constant, ω_D denotes the Debye frequency, and ω_p stands for the plasma frequency [65]). Despite rough treatment of complex electron-electron and electron-phonon processes, we were able to reproduce qualitatively the data considering the convexity in $\rho(T)$ as well as the maximum observed for ZnCrSb. Parameters resulting from the least-squares refinement are gathered in Table I. Due to much simpler temperature dependencies of $\rho(T)$ for ZnNiSb and ZnMnSb before the anomaly in 312 K, we applied the classical Bloch-Grüneisen formula without the Mott's term. Decent agreement with the experimental data was achieved in the whole temperature range.

For the ZrSiS phases in the lowest-temperature regime, we do not observe constant ρ resulting from the point defect and grain boundaries, but instead we see an increase in ρ values with decreasing temperature (see insets in Fig. 7). This anomalous behavior is usually attributed either to the Kondo effect corresponding to anomalously large scattering of conduction electrons on magnetic impurities [66] or to low-temperature effects resulting from the structural disorder. The most prominent phenomenon from the second group is the Altshuler-Aronov (AA) correction to electron-electron interactions [67]. This effect emerges at low temperatures, in disordered materials where the elastic scattering rate, e.g., due to collisions of charge carriers with lattice imperfections, dominates the inelastic processes. In this regime, the motion of electrons is diffusive. Electron-electron interaction in such systems leads to depletion of the density of states (the so-called Coulomb dip), implying minimum formation in the temperature dependence of electrical resistivity. The Altshuler-Aronov effect is not sensitive to the magnetic field. The readers are referred to Refs. [68–70] for detailed reports on this phenomenon and to Refs. [71–73] for more of exemplary bulk materials showing such behavior.

In order to clarify, for the Zn*X*Sb family, whether we observe the Kondo effect or AA correction, a magnetic field was applied to the resistivity measurements. The former effect is very field sensitive—polarization of magnetic moments localized on impurities virtually eliminates the Kondo scattering of conduction electrons. From the insets in Fig. 7, it is clear that a magnetic field up to 9 T does not destroy the minimum in $\rho(T)$, which suggests that electrical resistivity in Zn*X*Sb phases at the lowest temperatures is determined by the AA effect. The highest onset temperature is observed for ZnFeSb ($T_{\min} = 24$ K). ZnNiSb does not show a signature of the Altshuler-Aronov behavior, which is in line with its high crystallographic order.

We also calculated the residual resistivity ratio (*RRR*) defined as the proportion of resistivity at room temperature (ρ_{300K}) and the smallest resistivity (ρ_0) in the low-temperature regime ($RRR = \frac{\rho_{300K}}{\rho_0}$; see Table I). Values of *RRR* are commonly used for the measure of the disorder, i.e., *RRR* decreases with rising number of lattice imperfections. The temperature dependence of point defect scattering is significantly weaker than that of electron-phonon interactions, which usually dominates scattering in ordered metal. Indeed, for Zn*X*Sb, we observe a clear tendency of *RRR* with number of vacancies acting as efficient charge scattering centers: *RRR* attains significantly lower values for ZrSiS-type compounds than the ordered phase ZnNiSb. The lowest *RRR* is observed for ZnFeSb.

When impurity phases present in our samples are considered, we do not expect a significant influence on the electrical properties. Their total content does not exceed 6.6 vol.% (see Sec. III A). The main phases are metals and almost all of the detected impurities are also metallic or semimetallic: Cr [74], Fe [75], Mn [76], Sb [77], NiSb [78], and CrSb [79]. For Fe_3Zn_{10}, electronic properties were not reported to the best of our knowledge, but based on elemental constituents, we also expect it to be rather metallic or semimetallic. Hence, the presence of the precipitations cannot drastically affect the charge carrier concentration of the main phases and—as a

result—are very unlikely to have a profound influence on the resistivity.

The following paragraph will allow for comparison of the current data with previous literature knowledge. The literature report for ZnMnSb shows resistivity of approximately 50 $\mu\Omega$m at 300 K with weak temperature dependence and kink from ferromagnetic ordering at 302 K [26]. Discrepancies of the literature values obtained previously with respect to those presented in the current work most likely originate from different kinds of crystallographic disorder, which is sensitive to the synthesis conditions. Larger values of ρ in the literature as well as a negative temperature coefficient of resistivity (TCR $= \frac{1}{\rho}\frac{d\rho}{dT}$) consistently indicate a larger amount of defects in the specimen from Ref. [26]. Also, the change of ordering temperature between the current study and literature report [26] by 11 K most likely results from a slightly different atomic arrangement between the previously reported material and that presented here. In the case of ZnFeSb, electrical resistivity was previously displayed in the range 30–300 K with a dip at 50 K for part of the measurements and values of 145 $\mu\Omega$m at 300 K [29]. Surprisingly high values of ρ were attributed to the low density of the cold-pressed specimen [29]. For ZnNiSb, only resistivity of 0.39 $\mu\Omega$m at 300 K and metallic character of resistivity were reported [80], which is in agreement by an order of magnitude with the results presented here. The recently discovered ZrSiS-type compound ZnVSb [22] was characterized by electrical resistivity attaining a value of 9.6 $\mu\Omega$m at 300 K, which is similar to other ZnXSb phases. Interestingly, instead of the expected metallicklike behavior, ρ of ZnVSb in the literature exhibited a complex curvature with an overall increase with decreasing temperature. Between 120 and 160 K, hysteresis in ρ was found, indicative of a fractional charge transfer metal-insulator transition [22], which shows that resistivity mechanisms in ZnVSb are qualitatively different with respect to other ZnXSb representatives. The differences might stem either from qualitatively different band structure with a narrow pseudogap in the proximity of Fermi level [22] and/or distinct type of crystallographic disorder (vacancies on V and Sb sites, instead on X and Zn sites for ZnXSb, X = Cr, Mn, Fe).

For a recap of the electronic properties, the studied compounds are metals with significant contribution from Mott's interband scattering. Electrical transport properties are correlated with the disorder. The compounds with an abundance of defects are characterized by low *RRR* values and display the Altshuler-Aronov effect. The lowest *RRR* and highest onset temperature of AA behavior is observed for ZnFeSb. The material free from disorder, ZnNiSb, exhibits significantly higher *RRR*; no signature of AA correction can be detected in the resistivity of this material.

D. Thermal properties

Experimental temperature dependencies of heat capacity (C_p) are shown in Fig. 8(a). For ZnXSb, X = Cr, Fe, Ni, the C_p attains a typical sigmoidal shape. Values at room temperature are in the proximity of predictions from the Dulong-Petit law, $3nR$ = 74.8 J mol^{-1} K^{-1}, where n corresponds to the number of atoms per formula unit and R denotes a universal gas constant. The large peak at 306 K appearing for ZnMnSb

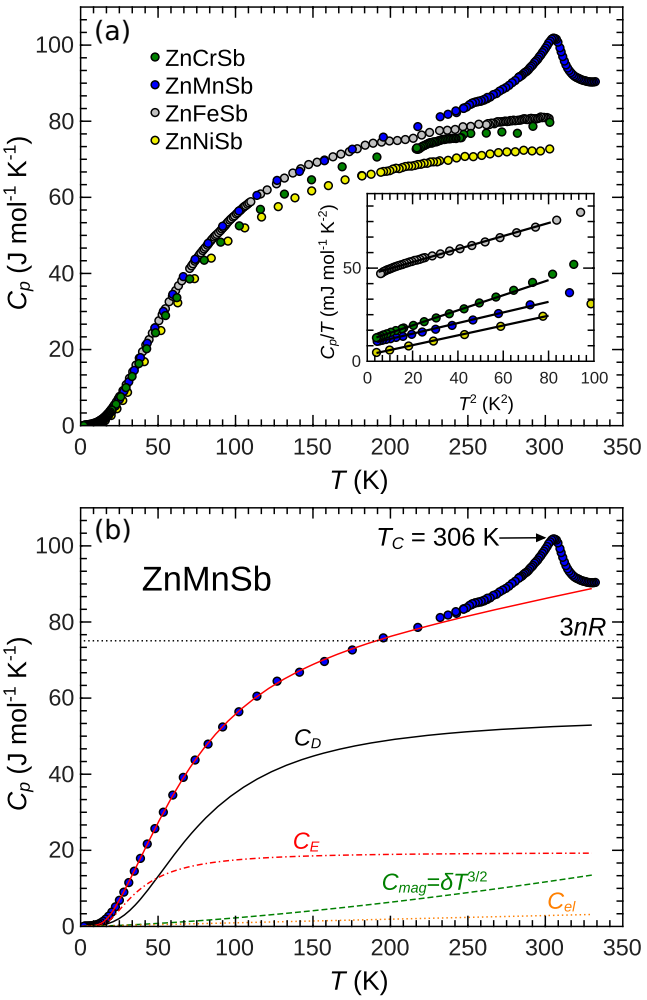

FIG. 8. (a) Temperature variation of heat capacity for ZnXSb phases, X = Cr, Mn, Fe, Ni. Dashed line corresponds to the Dulong-Petit limit. Inset shows the low-temperature data in C_p/T vs T^2 representation. Solid lines represent Debye fits—see text for details. (b) Results of fitting of Eq. (4) to the data for ZnMnSb. Red solid line corresponds to full Debye-Einstein fit; black solid and red dash-dotted curves stand for Debye and Einstein contributions, respectively; green dotted line denotes magnon heat capacity; and orange dotted line is the electronic contribution.

corresponds to the ferromagnetic ordering anomaly, a hint of which was also observed in the electrical resistivity [cf. Fig. 7(b)].

Below 9 K, we performed Debye fits with equation

$$C_p = \gamma T + \beta T^3, \tag{3}$$

where $\Theta_D^* = \sqrt[3]{\frac{12\pi^4}{\beta}nR}$; γ denotes the Sommerfeld coefficient and Θ_D^* stands for the Debye temperature relevant for the low-temperature regime. For the results, see the inset of Fig. 8(a) and Table II. Previous measurements of low-temperature specific heat have shown similar values of the Sommerfeld coefficient (11.3 mJ mol^{-1} K^{-2}) to our current findings [26]. The values of γ were used for obtaining the experimental density of states at the Fermi level (N_{E_F}) with formula $\gamma = \frac{1}{3}\pi^2 k_B^2 N_{E_F}$ (Table S4 in the SM [49]). The

TABLE II. Parameters resulting from heat-capacity analysis: Sommerfeld coefficient γ and Debye temperature relevant for low-temperature regime Θ_D^* from Eq. (3), fit parameters from Debye-Einstein model [Eq. (4): Debye and Einstein temperatures Θ_D, Θ_E, weight coefficient m, and anharmonicity factors α_D, α_E]; temperature of maximum in C_p/T^3 vs T plot, $T_{\max}$. The numbers in the parentheses are uncertainties obtained from least-square fitting.

Compound	γ (mJ mol^{-1}K^{-2})	Θ_D^* (K)	Θ_D (K)	Θ_E (K)	m	α_D (10^{-4} K^{-1})	α_E (10^{-4} K^{-1})	δ (mJ mol^{-1}K$^{1/2}$)	$T_{\max}$ (K)
ZnCrSb	11.3(1)	245(1)	345 (7)	99(2)	0.24(1)	2.34(4)	0.9(1)		14.2
ZnMnSb	9.52(5)	283(1)	315(4)	112(2)	0.26(2)	1.8(1)	1.0(2)	1.27(6)	23.1
ZnFeSb	47.6(7)	253(3)	308(2)	96(3)	0.18(1)				21.5
ZnNiSb	3.4(2)	280(2)	353(5)	124(3)	0.29(2)				20.2

experimental N_{E_F} for ZnCrSb and ZnNiSb is close to the predictions from *ab initio* techniques (also, Table S4 in the SM [49]). For ZnMnSb, however, regardless of the approach to spin arrangement, the density of states at the Fermi level is significantly enhanced with respect to calculations, which might suggest the presence of electron-electron or electron-phonon interactions. A similar observation was reported for these compounds in previous literature [33]. Interestingly, ZnFeSb, which is assumed to be the most disordered (unstable) phase from the series (see Secs. III A and III C), shows the biggest discrepancy between experimental and theoretical N_{E_F}—the enhancement of the N_{E_F} with respect to theory is as high as 10-fold. Previously, such a phenomenon due to disorder was reported for a number of cerium-, ytterbium-, and uranium-based compounds [81]. The most likely mechanism causing this behavior was the irregular environment around magnetic ions (Ce, Yb, U), which caused spin-glass-like behavior. Such scenario appears likely for the case of ZnFeSb due to its severe structural instability. Alternatively, enhancement of the Sommerfeld coefficient might be interpreted as an indication of strong electron-electron interactions; see e.g., Refs. [82,83]. Follow-up studies with a single crystal focused primarily on magnetic properties are necessary to clarify this interesting situation.

Further on, heat capacity was analyzed with the Debye-Einstein model corrected for anharmonicity [84],

$$C_p(T) = \gamma T + (1-w)\frac{C_D(T)}{1-\alpha_D T} + w\frac{C_E(T)}{1-\alpha_E T}, \quad (4)$$

$$C_D = 9nR\left(\frac{T}{\Theta_D}\right)^3 \int_0^{\Theta_D/T} \frac{x^4 \exp(x)}{[\exp(x)-1]^2} dx, \quad (5)$$

$$C_E = 3nR\left(\frac{\Theta_E}{T}\right)^2 \left[\exp\left(\frac{\Theta_E}{T}\right) - 1\right]^{-2} \exp\left(\frac{\Theta_E}{T}\right), \quad (6)$$

where Θ_D and Θ_E stand for Debye and Einstein temperatures, respectively, m denotes the weight coefficient, while α_D and α_E correspond to anharmonicity factors for Debye and Einstein modes, respectively. For ZnMnSb, we added a simple term describing the contribution from ferromagnetic magnons [85],

$$C_p(T) = \gamma T + (1-w)\frac{C_D(T)}{1-\alpha_D T} + w\frac{C_E(T)}{1-\alpha_E T} + C_{\text{magn}}, \quad (7)$$

where

$$C_{\text{magn}} = \delta T^{3/2}. \quad (8)$$

During fitting Eq. (4) to the heat-capacity data for ZnXSb, X = Cr, Mn, Ni, Sommerfeld coefficients were fixed to the values obtained from Eq. (3). In the case of ZnFeSb, due to the enhanced Sommerfeld coefficient at low temperature, which is unlikely to properly reflect the electronic contribution to heat capacity until 300 K, we refined γ during fitting of Eq. (4). The obtained γ in this case was equal to 32.7(2) mJ mol^{-1} K^{-2}. All other parameters resulting from least-squares fitting of Eq. (4) are gathered in Table II. The Debye-Einstein model correctly describes the heat-capacity data in the whole temperature range measured. Graphical presentation of the results obtained for ZnMnSb is depicted in Fig. 8(b), while for the remaining compounds, the reader is referred to Figs. S10(a)– S10(d) in the SM [49]. The validity of the Θ_E calculations is also confirmed by the C_p/T^3 vs T plot; see insets to Figs. S10(a)–S10(d) in the SM [49]. As expected, the temperature of the maximum ($T_{\max}$) in the so-derived curves is related to the Einstein temperature as $5T_{\max} \approx \Theta_E$ [22].

Anharmonicity factors for ZnCrSb and ZnMnSb attain sizable values similar to those reported in the literature for other intermetallics [86,87]. Anharmonic contribution to heat capacity might be speculatively associated with crystallographic disorder [88], which indeed was found for these three phases via pXRD analysis. As expected, in the case of ZnNiSb, for which we did not find any considerable disorder, α_D and α_E converge to zero. Analysis of anharmonicity was not available for ZnFeSb due to the fact that the relaxed Sommerfeld coefficient had a similar mathematic impact on the modeled curve from Eq. (4).

E. Magnetic properties

Measurements of magnetic susceptibility are displayed in Figs. S11(a)–S11(d) in the SM [49]. ZnMnSb exhibits clear ferromagnetic ordering in temperature corresponding to anomalies in heat capacity and electrical resistivity—308 K is read from the half of the slope in $\chi(T)$. The temperature of ferromagnetic ordering for this compound in the literature (302 K) [26] is similar to the result presented here. Calculation of magnetic moment 2 K from the saturation of the magnetization gives 2.21μ_B per Mn atom with experimental composition $Zn_{0.97}Mn_{0.92}Sb$, which is reduced with respect to the conventional moment expected for the Mn atom (5.92 μ_B).

ZnFeSb in the current studies shows paramagnetic behavior of the matrix and anomalies, which most likely result from ordering of the impurities; see Fig. S11(c) in the SM [49]. In such scenario, the tiny amount of contaminants

would order ferromagnetically at 290 K and antiferromagnetically at 17 K. Binary iron compounds are known to attain both ferromagnetic (e.g., $FeSb_2$ [89]) and antiferromagnetic (e.g., $Fe_{1+\delta}Sb$ [90]) spin configurations. A previous report on ZnFeSb showed similar results to our temperature dependence of susceptibility. The compound, however, was described as a ferromagnet with ordering with $T_C = 275$ K, magnetic cluster state formation at 70 K, and likely spin-glass signal occurring at 30 K [29]. However, no corresponding anomalies expected for these phenomena [91] in heat capacity and electrical resistivity [29] were noticed in our data, which leads us to suggest that the additional signal in $\chi(T)$ for ZnFeSb might be explained by the simpler scenario mentioned above—ordering of the minuscule amount of contaminants.

All the remaining ZnXSb phases in the current study seem to show behavior qualitatively similar to that of ZnFeSb: paramagnetic matrix down to the lowest temperature studied and additional signal which can be ascribed to ordering of the contaminant. For ZnCrSb, the impurities would order antiferromagnetically at 235 and 20 K (Fig. S11(a) in the SM [49]), while the additional signal for the ZnNiSb sample at approximately 290 and 230 K would correspond to ferromagnetic ordering; see Fig. S11(d) in the SM [49]. We found identifying the anomalies to a particular precipitation rather difficult. One of the origins of the troublesome situation is that the signal of the magnetically ordered compound can be several orders of magnitude larger than from the paramagnet, which explains why we could not detect the responsible impurities during structural studies—their concentration might be as low as several ppm to be already detectable. Additionally, the bulk magnetic properties constituting the majority of the literature report might significantly differ from those for tiny objects such as thin films on grain boundaries or several unit-cell-wide precipitations, which can present in bulk samples. For example, $NiSb_2$ is known to be diamagnetic in bulk form, but nanocrystals of this composition are ferromagnetic [92]. No anomalous thermal hysteresis was detected by taking cooling and heating susceptibility cycles.

As the last part of the research, we performed exploratory magnetic calculations assuming the possibility of localized magnetic moments for all three ZnXSb compounds. The calculations were performed with scenarios where a ferromagnetic ordering and two possible antiferromagnetic configurations were checked (checkerboard and layered—see Fig. S12 in the SM [49]). The obtained localized magnetic moments for ZnXSb, X = Cr, Mn, Fe, are lower than the expectations for these elements in most of their oxidation states; see Table S5 in the SM [49]. This finding is consistent with the general expectations for ZrSiS-type compounds to show the partially delocalized character of magnetism [31]. ZnNiSb shows no localized magnetic moment due to the completely filled d-electron shell of Ni.

Table S6 in the SM [49] displays the results of the total energies of each material in three different scenarios considered before. For most of the studied compounds, the energy differences are rather minuscule: slight preference for ferromagnetism in ZnCrSb, and antiferromagnetism in ZnFeSb. The only clear preference is that of ferromagnetic order over the layered antiferromagnetic configuration for ZnMnSb. Small differences in total energy between different types of long-range order in a localized scenario imply possibilities of spin fluctuations, similarly to the case of ZnVSb [22].

Here, it is necessary to remind the reader that the literature approach to the studied family of compounds is usually underlining the at least partially itinerant character of magnetism [22,31–33]. Hence, the performed calculations in the localized scenario might provide only part of the picture regarding complex magnetic interaction in ZnXSb materials. This seems to be particularly clear for the case of ZnMnSb, which in the experiment shows strong, high-temperature ferromagnetism with reduced values of magnetic moment on Mn (see above). The calculations, in turn, provide us with a rather intense competition between ferro- and antiferromagnetic configurations. To make sure we do not suffer from technical problems, a series of magnetic calculations was performed under different conditions (variety of Hubbard corrections values, different initial magnetic moments, and considering the influence of the presence of Mn vacancies—see Table S7 in the SM [49]). In the vast majority of the results, the energy difference between ferro- and antiferromagnetic ordering was small (below 0.5 eV/f.u.) and showed a preference for antiferromagnetic order. The discrepancy between theory and experiment confirms that a localized scenario cannot be considered a sufficient explanation for magnetism in ZnMnSb. Further research involving single-crystal studies, including more sophisticated experiments such as neutron diffraction and transport measurements, preferentially even to temperatures lower than 2 K, might provide further insight into magnetic interaction in this curious family of compounds.

IV. SUMMARY

We investigated the structural, magnetotransport, and thermodynamic properties of phases ZnXSb, X = Cr, Mn, Fe, where ZnCrSb is a newly discovered compound. The phases based on chromium, manganese, and iron were found to exhibit a sizable amount of vacancies on transition-metal sites. The performed studies suggest that the disorder rises towards heavier mass of transition metal X, manifesting most profoundly in the case of ZnFeSb. This finding is in line with the previous literature showing the existence of three polymorphic modifications of ZnFeSb, which suggests that the compound is on the very edge of structural instability. Materials with transition metal X heavier than ZnXSb, X = Fe, are thus unlikely to crystallize in a ZrSiS-type cell. As indicated by COHP calculations, the most pronounced point defects in ZrSiS-type compounds (vacancies on X site) originate primarily from antibonding interaction on the 2D sublattice formed by X atoms. The results obtained for the disordered materials were compared with a chemically similar phase ZnNiSb attaining MgAgAs-type structure. In this compound, X = Ni are separated by a large distance (approximately 4.2 Å) and show no repulsive X-X interaction in ZnNiSb, as indicated by COHP calculations. Accordingly, virtually no crystallographic defects are found for ZnNiSb. The atomic displacement parameters seem to correlate with disorder. Compounds with a large amount of structural imperfections show significantly higher values of B_{iso}. From an electrical perspective, phases ZnXSb, X = Cr, Mn, Fe,

show a low residual resistivity ratio (1.24–1.66) and Altshuler-Aronov correction to Coulomb interaction. The observations are in line with the expected severe scattering of electrons on point defects of the crystal lattice. The residual resistivity ratio for ZnNiSb is significantly bigger than in the case of the studied disordered phases. ZnNiSb also shows no traces of the AA effect. Heat-capacity studies revealed that ZnFeSb shows a 10-fold enhancement in the Sommerfeld coefficient with respect to *ab initio* calculations, which might be correlated to its structural instability. From the perspective of magnetism, we clarified that all the studied compounds, except ZnMnSb, do not exhibit any long-range magnetic order down to 2 K. Manganese-based material is a high-temperature ferromagnet ($T_C = 302$ K). Reduced value of the magnetic moment ($2.21\mu_B$/Mn atom) with respect to the value expected for Mn in the localized scenario, as well as a series of *ab initio* calculations, indicate that magnetism in ZnMnSb is of a partially itinerant character. The family of Zn*X*Sb compounds seems to be a curious topic for further, more advanced studies focused on magnetism. We also hope that the presented analysis will be useful for materials in which structural imperfections are influencing the electrical transport.

ACKNOWLEDGMENTS

E.S.T. acknowledges funding from Project No. NSF DMR 1555340. K.C. kindly acknowledges support from the Internal Travel Grant from the Institute of Low Temperature and Structure Research, Polish Academy of Sciences (Poland).

[1] C. Wang, T. Yang, C. L. Tracy, C. Lu, H. Zhang, Y.-J. Hu, L. Wang, L. Qi, L. Gu, Q. Huang *et al.*, Disorder in $M_{n+1}AX_n$ phases at the atomic scale, Nat. Commun. **10**, 622 (2019).

[2] D. Chaney, A. Castellano, A. Bosak, J. Bouchet, F. Bottin, B. Dorado, L. Paolasini, S. Rennie, C. Bell, R. Springell, and G. H. Lander, Tuneable correlated disorder in alloys, Phys. Rev. Mater. **5**, 035004 (2021).

[3] H. Xie, H. Wang, C. Fu, Y. Liu, G. J. Snyder, X. Zhao, and T. Zhu, The intrinsic disorder related alloy scattering in ZrNiSn half-Heusler thermoelectric materials, Sci. Rep. **4**, 6888 (2014).

[4] H. Wang, A. D. LaLonde, Y. Pei, and G. J. Snyder, The criteria for beneficial disorder in thermoelectric solid solutions, Adv. Funct. Mater. **23**, 1586 (2013).

[5] F. Gascoin and A. Maignan, Order-disorder transition in $AgCrSe_2$: A new route to efficient thermoelectrics, Chem. Mater. **23**, 2510 (2011).

[6] X. Ni, G. Liang, J.-S. Wang, and B. Li, Disorder enhances thermoelectric figure of merit in armchair graphane nanoribbons, Appl. Phys. Lett. **95**, 192114 (2009).

[7] S. N. Guin and K. Biswas, Cation disorder and bond anharmonicity optimize the thermoelectric properties in kinetically stabilized rocksalt $AgBiS_2$ nanocrystals, Chem. Mater. **25**, 3225 (2013).

[8] D. Li, H. Zhao, S. Li, B. Wei, J. Shuai, C. Shi, X. Xi, P. Sun, S. Meng, L. Gu *et al.*, Atomic disorders induced by silver and magnesium ion migrations favor high thermoelectric performance in α-MgAgSb-based materials, Adv. Funct. Mater. **25**, 6478 (2015).

[9] I. Pallecchi, M. Pani, F. Ricci, S. Lemal, D. I. Bilc, P. Ghosez, C. Bernini, N. Ardoino, G. Lamura, and D. Marré, Thermoelectric properties of chemically substituted full-Heusler $Fe_2TiSn_{1-x}Sb_x$ ($x = 0$, 0.1, and 0.2) compounds, Phys. Rev. Mater. **2**, 075403 (2018).

[10] L. L. Baranowski, K. McLaughlin, P. Zawadzki, S. Lany, A. Norman, H. Hempel, R. Eichberger, T. Unold, E. S. Toberer, and A. Zakutayev, Effects of Disorder on Carrier Transport in Cu_2SnS_3, Phys. Rev. Appl. **4**, 044017 (2015).

[11] J. J. Scragg, J. K. Larsen, M. Kumar, C. Persson, J. Sendler, S. Siebentritt, and C. Platzer Björkman, Cu-Zn disorder and band gap fluctuations in $Cu_2ZnSn(S, Se)_4$: Theoretical and experimental investigations, Phys. Status Solidi B **253**, 247 (2016).

[12] B. G. Mendis, M. D. Shannon, M. C. Goodman, J. D. Major, R. Claridge, D. P. Halliday, and K. Durose, Direct observation of Cu, Zn cation disorder in Cu_2ZnSnS_4 solar cell absorber material using aberration corrected scanning transmission electron microscopy, Prog. Photovolt. Res. Appl. **22**, 24 (2014).

[13] C. Brun, T. Cren, V. Cherkez, F. Debontridder, S. Pons, D. Fokin, M. Tringides, S. Bozhko, L. Ioffe, B. Altshuler *et al.*, Remarkable effects of disorder on superconductivity of single atomic layers of lead on silicon, Nat. Phys. **10**, 444 (2014).

[14] A. P. Mackenzie, R. K. W. Haselwimmer, A. W. Tyler, G. G. Lonzarich, Y. Mori, S. Nishizaki, and Y. Maeno, Extremely Strong Dependence of Superconductivity on Disorder in Sr_2RuO_4, Phys. Rev. Lett. **80**, 161 (1998).

[15] J. Freudenberger, S.-L. Drechsler, G. Fuchs, A. Kreyssig, K. Nenkov, S. Shulga, K.-H. Müller, and L. Schultz, Superconductivity and disorder in $Y_xLu_{1-x}Ni_2B_2C$, Phys. C: Superconduct. **306**, 1 (1998).

[16] T. R. Kirkpatrick and D. Belitz, Disorder-Induced Triplet Superconductivity, Phys. Rev. Lett. **66**, 1533 (1991).

[17] C. Liu, W. Gao, B. Yang, and S. Zhang, Disorder-Induced Topological State Transition in Photonic Metamaterials, Phys. Rev. Lett. **119**, 183901 (2017).

[18] B. Leung and E. Prodan, Effect of strong disorder in a three-dimensional topological insulator: Phase diagram and maps of the Z_2 invariant, Phys. Rev. B **85**, 205136 (2012).

[19] J. Song, H. Liu, H. Jiang, Q. F. Sun, and X. C. Xie, Dependence of topological Anderson insulator on the type of disorder, Phys. Rev. B **85**, 195125 (2012).

[20] S. A. A. Ghorashi, S. Davis, and M. S. Foster, Disorder-enhanced topological protection and universal quantum criticality in a spin-$\frac{3}{2}$ topological superconductor, Phys. Rev. B **95**, 144503 (2017).

[21] T. Cichorek, D. Gnida, R. Niewa, A. Schlechte, M. Schmidt, Y. Prots, R. Ramlau, Z. Henkie, R. Kniep, and F. Steglich, Resistivity anomaly in structurally disordered PbFCl-type arsenide selenides, J. Low Temp. Phys. **147**, 309 (2007).

[22] E. A. Bensen, K. Ciesielski, L. C. Gomes, B. R. Ortiz, J. Falke, O. Pavlosiuk, D. Weber, T. L. Braden, K. X. Steirer, D. Szymanski, J. E. Goldberger, C. Y. Kuo, C. T. Chen, C. F. Chang, L. H. Tjeng, D. Kaczorowski, E. Ertekin, and E. S.

Toberer, Anomalous electronic properties in layered, disordered znvsb, Phys. Rev. Mater. **5**, 015002 (2021).

[23] M. W. Gaultois, A. P. Grosvenor, P. E. Blanchard, and A. Mar, Ternary arsenides $Zr(Si_xAs_{1-x})As$ with $PbCl_2$-type ($0 \leqslant x \geqslant 0.4$) and PbFCl-type ($x = 0.6$) structures, J. Alloys Compd. **492**, 19 (2010).

[24] S. Ishida, H. Fujihisa, I. Hase, Y. Yanagi, K. Kawashima, K. Oka, Y. Gotoh, Y. Yoshida, A. Iyo, H. Eisaki *et al.*, Superconductivity in layered $ZrP_{2-x}Se_x$ with PbFCl-type structure, Supercond. Sci. Technol. **29**, 055004 (2016).

[25] L. M. Schoop, M. N. Ali, C. Straßer, A. Topp, A. Varykhalov, D. Marchenko, V. Duppel, S. S. Parkin, B. V. Lotsch, and C. R. Ast, Dirac cone protected by non-symmorphic symmetry and three-dimensional Dirac line node in ZrSiS, Nat. Commun. **7**, 11696 (2016).

[26] V. Johnson and W. Jeitschko, Ferromagnetic anti-PbFCl-type ZnMnSb, J. Solid State Chem. **22**, 71 (1977).

[27] I. Chumak, V. Pavlyuk, G. Dmytriv, and J. Stepień-Damm, Phase equilibria and crystal structure of compounds in the Fe–Zn–Sb system at 570 K, J. Alloys Compd. **307**, 223 (2000).

[28] C.-W. T. Lo, T. Kolodiazhnyi, S. Song, Y.-C. Tseng, and Y. Mozharivskyj, Experimental survey of dopants in $Zn_{13}Sb_{10}$ thermoelectric material, Intermetallics **123**, 106831 (2020).

[29] D.-B. Xiong and Y. Zhao, Half-Heusler phase related structural perturbations near stoichiometric composition FeZnSb, J. Solid State Chem. **184**, 1159 (2011).

[30] D.-B. Xiong, Y. Zhao, N. L. Okamoto, C. Pietzonka, T. Waki, and H. Inui, $Ru_9Zn_7Sb_8$: A structure with a $2 \times 2 \times 2$ supercell of the half-Heusler phase, Inorg. Chem. **49**, 10536 (2010).

[31] K. Motizuki, H. Ido, T. Itoh, and M. Morifuji, Itinerant electron theory of magnetism of Cu_2Sb-type compounds, in *Electronic Structure and Magnetism of 3d-Transition Metal Pnictides*, edited by R. Hull, C. Jagadish, R. M. Osgood Jr., J. Parisi, Z. Wang, and H. Warlimont (Springer, New York, 2009), pp. 127–138.

[32] P. A. Murgatroyd, K. Routledge, S. Durdy, M. W. Gaultois, T. W. Surta, M. S. Dyer, J. B. Claridge, S. N. Savvin, D. Pelloquin, S. Hébert *et al.*, Chemically controllable magnetic transition temperature and magneto-elastic coupling in MnZnSb compounds, Adv. Funct. Mater. **31**, 2100108 (2021).

[33] T. Kanomata, H. Endo, S. Mori, H. Okajima, T. Hihara, K. Sumiyama, T. Kaneko, and K. Suzuki, Specific heat of mnalge, mngage and mnznsb, J. Magn. Magn. Mater. **140-144**, 133 (1995).

[34] J. Rodríguez-Carvajal, Recent advances in magnetic structure determination by neutron powder diffraction, Phys. B: Condens. Matter **192**, 55 (1993).

[35] G. Kresse and J. Furthmüller, Efficient iterative schemes for ab initio total-energy calculations using a plane-wave basis set, Phys. Rev. B **54**, 11169 (1996).

[36] J. P. Perdew, K. Burke, and M. Ernzerhof, Generalized Gradient Approximation Made Simple, Phys. Rev. Lett. **77**, 3865 (1996).

[37] P. E. Blöchl, Projector augmented-wave method, Phys. Rev. B **50**, 17953 (1994).

[38] H. J. Monkhorst and J. D. Pack, Special points for Brillouin-zone integrations, Phys. Rev. B **13**, 5188 (1976).

[39] A. M. Ganose, A. J. Jackson, and D. O. Scanlon, Sumo: Command-line tools for plotting and analysis of periodic *ab initio* calculations, JOSS **3**, 717 (2018).

[40] S. L. Dudarev, G. A. Botton, S. Y. Savrasov, C. J. Humphreys, and A. P. Sutton, Electron-energy-loss spectra and the structural stability of nickel oxide: An LSDA+U study, Phys. Rev. B **57**, 1505 (1998).

[41] S. Lutfalla, V. Shapovalov, and A. T. Bell, Calibration of the DFT/GGA+U method for determination of reduction energies for transition and rare earth metal oxides of Ti, V, Mo, and Ce, J. Chem. Theory Comput. **7**, 2218 (2011).

[42] C. Weber, D. D. O'Regan, N. D. M. Hine, M. C. Payne, G. Kotliar, and P. B. Littlewood, Vanadium Dioxide: A Peierls-Mott Insulator Stable against Disorder, Phys. Rev. Lett. **108**, 256402 (2012).

[43] E. Goh, J. Mah, and T. Yoon, Effects of Hubbard term correction on the structural parameters and electronic properties of wurtzite ZnO, Comput. Mater. Sci. **138**, 111 (2017).

[44] M. B. Kanoun, S. Goumri-Said, U. Schwingenschlögl, and A. Manchon, Magnetism in Sc-doped ZnO with zinc vacancies: A hybrid density functional and GGA+U approaches, Chem. Phys. Lett. **532**, 96 (2012).

[45] V. L. Deringer, A. L. Tchougréeff, and R. Dronskowski, Crystal orbital Hamilton population (COHP) analysis as projected from plane-wave basis sets, J. Phys. Chem. A **115**, 5461 (2011).

[46] S. Steinberg and R. Dronskowski, The crystal orbital Hamilton population (COHP) method as a tool to visualize and analyze chemical bonding in intermetallic compounds, Crystals **8**, 225 (2018).

[47] S. Maintz, V. L. Deringer, A. L. Tchougréeff, and R. Dronskowski, Lobster: A tool to extract chemical bonding from plane-wave based DFT, J. Comput. Chem. **37**, 1030 (2016).

[48] S. Maintz, V. L. Deringer, A. L. Tchougréeff, and R. Dronskowski, Analytic projection from plane-wave and PAW wave functions and application to chemical-bonding analysis in solids, J. Comput. Chem. **34**, 2557 (2013).

[49] See Supplemental Material at http://link.aps.org/supplemental/10.1103/PhysRevMaterials.6.063602 for further information about details of crystal structures, COHP calculations, electronic band structures, heat capacity, and magnetization data, as well as theoretical calculations regarding magnetic properties.

[50] D.-B. Xiong, N. L. Okamoto, T. Waki, Y. Zhao, K. Kishida, and H. Inui, High-T_C ferromagnetic semiconductor-like behavior and unusual electrical properties in compounds with a $2 \times 2 \times 2$ superstructure of the half-Heusler phase, Chem. Eur. J. **18**, 2536 (2012).

[51] I. Chumak and V. Pavlyuk, Interaction of the components in the Ni–Zn–Sb ternary system at 570 K, J. Alloys Compd. **367**, 85 (2004).

[52] V. Dymont, G. Makovetskii, and V. Ryzhkovskii, Neutron diffraction determination of Mn and Zn structure positions in MnZnSb, Phys. Status Solidi A **107**, K89 (1988).

[53] M. Wuttig, D. Lüsebrink, D. Wamwangi, W. Wełnic, M. Gilleßen, and R. Dronskowski, The role of vacancies and local distortions in the design of new phase-change materials, Nat. Mater. **6**, 122 (2007).

[54] B. Koley, N. Roy, Harshit, S. Mallick, A. Simonov, and P. P. Jana, A vacancy-driven intermetallic phase: Rh_3Cd_5-δ ($\delta \approx 0.56$), Inorg. Chem. **60**, 5488 (2021).

[55] S. Lany and A. Zunger, Accurate prediction of defect properties in density functional supercell calculations, Model. Simul. Mater. Sci. Eng. **17**, 084002 (2009).

[56] Z. Hou, Y. Wang, G. Xu, X. Zhang, E. Liu, W. Wang, Z. Liu, X. Xi, W. Wang, and G. Wu, Transition from semiconducting to metallic-like conducting and weak antilocalization effect in single crystals of LuPtSb, Appl. Phys. Lett. **106**, 102102 (2015).

[57] C. Shekhar, S. Ouardi, A. K. Nayak, G. H. Fecher, W. Schnelle, and C. Felser, Ultrahigh mobility and nonsaturating magnetoresistance in Heusler topological insulators, Phys. Rev. B **86**, 155314 (2012).

[58] K. Gofryk, D. Kaczorowski, T. Plackowski, A. Leithe-Jasper, and Y. Grin, Magnetic and transport properties of rare-earth-based half-Heusler phases *R*PdBi: Prospective systems for topological quantum phenomena, Phys. Rev. B **84**, 035208 (2011).

[59] N. Mott, A discussion of the transition metals on the basis of quantum mechanics, Proc. Phys. Soc. **47**, 571 (1935).

[60] N. F. Mott, The electrical conductivity of transition metals, Proc. R. Soc. London, Ser. A **153**, 699 (1936).

[61] C. Wei, N. Antolin, O. D. Restrepo, W. Windl, and J.-C. Zhao, A general model for thermal and electrical conductivity of binary metallic systems, Acta Mater. **126**, 272 (2017).

[62] T. Shang, W. Xie, D. J. Gawryluk, R. Khasanov, J. Zhao, M. Medarde, M. Shi, H. Yuan, E. Pomjakushina, and T. Shiroka, Multigap superconductivity in the Mo_5PB_2 boron–phosphorus compound, New J. Phys. **22**, 093016 (2020).

[63] K. Ciesielski, G. Chajewski, M. Samsel-Czekała, A. Hackemer, P. Obstarczyk, A. Pikul, and D. Kaczorowski, Electronic properties of $LaTE_2Ge_2$ (TE = Fe, Co, Ni, Cu and Ru), Solid State Commun. **280**, 13 (2018).

[64] M. Schmidt, T. Cichorek, R. Niewa, A. Schlechte, Y. Prots, F. Steglich, and R. Kniep, Crystallographic disorder and electron scattering on structural two-level systems in zras1. 4se0. 5, J. Phys.: Condens. Matter **17**, 5481 (2005).

[65] P. B. Allen, *Quantum Theory of Real Materials*, edited by J. R. Chelikowsky and S. G. Louie (Kluwer Academic Publishers, Boston, 1996), Chap. 17.

[66] J. Kondo, Resistance minimum in dilute magnetic alloys, Prog. Theor. Phys. **32**, 37 (1964).

[67] B. Altschuler and A. Aronov, *Electron-Electron Interactions in Disordered Systems*, edited by A. L. Efros and M. Pollak (Elsevier, Amsterdam, 1985), Vol. 27.

[68] A. E. White, M. Tinkham, W. J. Skocpol, and D. C. Flanders, Evidence for Interaction Effects in the Low-Temperature Resistance Rise in Ultrathin Metallic Wires, Phys. Rev. Lett. **48**, 1752 (1982).

[69] F. Pierre, A. B. Gougam, A. Anthore, H. Pothier, D. Esteve, and N. O. Birge, Dephasing of electrons in mesoscopic metal wires, Phys. Rev. B **68**, 085413 (2003).

[70] P. M. Echternach, M. E. Gershenson, H. M. Bozler, A. L. Bogdanov, and B. Nilsson, Temperature dependence of the resistance of one-dimensional metal films with dominant Nyquist phase breaking, Phys. Rev. B **50**, 5748 (1994).

[71] M. Kobayashi, K. Tanaka, A. Fujimori, S. Ray, and D. D. Sarma, Critical Test for Altshuler-Aronov Theory: Evolution of the Density of States Singularity in Double Perovskite Sr_2FeMoO_6 with Controlled Disorder, Phys. Rev. Lett. **98**, 246401 (2007).

[72] D. Gnida, K. Ciesielski, and D. Kaczorowski, Origin of the negative temperature coefficient of resistivity in the half-Heusler antimonides LuNiSb and YPdSb, Phys. Rev. B **103**, 174206 (2021).

[73] K. Ciesielski, D. Gnida, H. Borrmann, R. Ramlau, Y. Prots, D. Szymański, Y. Grin, and D. Kaczorowski, Structural, thermodynamic and magnetotransport properties of half-Heusler compound HoPtSb, J. Alloys Compd. **829**, 154467 (2020).

[74] P. E. S. Persson and L. I. Johansson, Bulk band structure of chromium, Phys. Rev. B **34**, 2284 (1986).

[75] T. Nautiyal and S. Auluck, Electronic structure of ferromagnetic iron: Band structure and optical properties, Phys. Rev. B **34**, 2299 (1986).

[76] P. D. Desai, H. James, and C. Y. Ho, Electrical resistivity of aluminum and manganese, J. Phys. Chem. Ref. Data **13**, 1131 (1984).

[77] L. Falicov and P. Lin, Band structure and Fermi surface of antimony: Pseudopotential approach, Phys. Rev. **141**, 562 (1966).

[78] M. Podgorny and C. Wijers, The band structure of NiSb, Solid State Commun. **34**, 233 (1980).

[79] J. Dijkstra, C. Van Bruggen, C. Haas, and R. de Groot, Electronic band-structure calculations of some magnetic chromium compounds, J. Phys.: Condens. Matter **1**, 9163 (1989).

[80] F. Rosi, J. Dismukes, and E. Hockings, Semiconductor materials for thermoelectric power generation up to 700 c, Electr. Eng. **79**, 450 (1960).

[81] K. Gschneidner Jr., J. Tang, S. Dhar, and A. Goldman, False heavy fermions, Phys. B: Condens. Matter **163**, 507 (1990).

[82] S. G. Stewart, Heavy-fermion systems, Rev. Mod. Phys. **56**, 755 (1984).

[83] K. Górnicka, D. Das, S. Gutowska, B. Wiendlocha, M. J. Winiarski, T. Klimczuk, and D. Kaczorowski, Iridium 5 *d*-electron driven superconductivity in $ThIr_3$, Phys. Rev. B **100**, 214514 (2019).

[84] C. A. Martin, Simple treatment of anharmonic effects on the specific heat, J. Phys.: Condens. Matter **3**, 5967 (1991).

[85] A. Tari, *The Specific Heat of Matter at Low Temperatures* (World Scientific, Singapore, 2003).

[86] P. Svoboda, P. Javorský, M. Diviš, V. Sechovský, F. Honda, G. Oomi, and A. A. Menovsky, Importance of anharmonic terms in the analysis of the specific heat of UNi_2Si_2, Phys. Rev. B **63**, 212408 (2001).

[87] K. Procházková, S. Danis, and P. Svoboda, Specific heat study of $PrNi_4Si$, Acta Phys. Pol. A **113**, 299 (2008).

[88] P. Zalden, K. S. Siegert, S. Rols, H. E. Fischer, F. Schlich, T. Hu, and M. Wuttig, Specific heat of $(GeTe)_x(Sb_2Te_3)_{1-x}$ phase-change materials: The impact of disorder and anharmonicity, Chem. Mater. **26**, 2307 (2014).

[89] P. Sun, M. Søndergaard, B. B. Iversen, and F. Steglich, Strong electron correlations in $FeSb_2$, Ann. Phys. **523**, 612 (2011).

[90] K. Yamaguchi, H. Yamamoto, Y. Yamaguchi, and H. Watanabe, Antiferromagnetism of $Fe_{1+\delta}Sb$, J. Phys. Soc. Jpn. **33**, 1292 (1972).

[91] V. K. Anand, D. T. Adroja, and A. D. Hillier, Ferromagnetic cluster spin-glass behavior in $PrRhSn_3$, Phys. Rev. B **85**, 014418 (2012).

[92] C. Li, J. Hu, Q. Peng, and X. Wang, Synthesis and characterization of nanocrystalline NiSb and $NiSb_2$ at low temperature, Mater. Chem. Phys. **110**, 106 (2008).